catalysts

MDPI

Article

Optimizing Charge Separation and Transport: Enhanced Photoelectrochemical Water Splitting in α-Fe_2O_3/CZTS Nanorod Arrays

Wen Chen [1,2], Ao-Sheng She [1,2], Ming-Hao Ji [2], Hao-Yan Shi [2], Yang Yang [2,3], Yi-Hu Pu [4], Rui Chen [1,2], Wei-Hua Yang [4], Yan-Xin Chen [1,2,5,6,*] and Can-Zhong Lu [1,2,5,6,*]

1 College of Chemistry, Fuzhou University, Fuzhou 350116, China
2 State Key Laboratory of Structural Chemistry, Fujian Institute of Research on the Structure of Matter, Chinese Academy of Sciences, Fuzhou 350002, China
3 College of Chemistry and Materials Science, Fujian Normal University, Fuzhou 350108, China
4 College of Materials Science and Engineering, Huaqiao University, Xiamen 361021, China
5 Xiamen Key Laboratory of Rare Earth Photoelectric Functional Materials, Xiamen Institute of Rare-Earth Materials, Haixi Institutes, Chinese Academy of Sciences, Xiamen 361021, China
6 Fujian Science and Technology Innovation Laboratory for Optoelectronic Information of China, Fuzhou 350108, China
* Correspondence: yanxinchen@fjirsm.ac.cn (Y.-X.C.); czlu@fjirsm.ac.cn (C.-Z.L.)

Abstract: This study explores the enhancement of α-Fe_2O_3 (hematite) nanorod arrays for photoelectrochemical applications by constructing a Cu_2ZnSnS_4 (CZTS) heterojunction. While α-Fe_2O_3 offers good stability, a low cost, and environmental benefits, its efficiency is limited by slow oxygen evolution kinetics, high carrier recombination rates, and low conductivity. By introducing CZTS, a material with strong light absorption and charge transport properties, we enhance the separation of photogenerated charge carriers, reduce charge transfer resistance, and increase the carrier concentration, thereby boosting the overall photoelectrochemical performance. The experimental results show that a modified FC-15 photoanode achieves a photocurrent density of 3.40 mA/cm^2 at 1.60 V vs. RHE, a substantial increase compared to 0.40 mA/cm^2 for unmodified α-Fe_2O_3. Band gap analysis reveals a reduced band gap in the FC-15 material, enhancing light absorption and boosting the photoelectrocatalytic performance. In photoelectrochemical water-splitting tests, the FC-15 photoanode achieves a hydrogen production rate of 41.6 μmol/cm^2/h, which is significantly improved over the unmodified sample at 5.64 μmol/cm^2/h. These findings indicate that the CZTS/α-Fe_2O_3 heterojunction effectively promotes charge separation, enhances charge transport, and improves light absorption, substantially increasing photocatalytic efficiency. This heterojunction approach offers new insights and technical strategies for developing photocatalytic materials with potential applications in renewable energy.

Keywords: photoelectrochemical water splitting; α-Fe_2O_3/CZTS heterojunction; charge separation and transport; photoelectrocatalytic efficiency

check for updates

Citation: Chen, W.; She, A.-S.; Ji, M.-H.; Shi, H.-Y.; Yang, Y.; Pu, Y.-H.; Chen, R.; Yang, W.-H.; Chen, Y.-X.; Lu, C.-Z. Optimizing Charge Separation and Transport: Enhanced Photoelectrochemical Water Splitting in α-Fe_2O_3/CZTS Nanorod Arrays. *Catalysts* **2024**, *14*, 812. https://doi.org/10.3390/catal14110812

Academic Editor: Helmut Schäfer

Received: 14 October 2024
Revised: 4 November 2024
Accepted: 6 November 2024
Published: 11 November 2024

Copyright: © 2024 by the authors. Licensee MDPI, Basel, Switzerland. This article is an open access article distributed under the terms and conditions of the Creative Commons Attribution (CC BY) license (https://creativecommons.org/licenses/by/4.0/).

1. Introduction

Researchers actively seek carbon-free alternatives such as hydrogen to address climate change and the energy crisis to replace fossil fuels. Photoelectrocatalytic water splitting, as an emerging technology, mimics natural photosynthesis by harnessing solar energy to drive the chemical reactions that split water into hydrogen and oxygen, thereby providing clean energy [1–3]. The success of this technology depends not only on the hydrogen generation capability of the photoelectrode under illumination, but also on the production of oxygen. Developing and optimizing semiconductor materials that meet the requirements for efficient water splitting remains a complex challenge [4]. Therefore, the research and improvement of photoelectrocatalytic materials with superior stability and high catalytic

efficiency have become a hot topic in scientific research. In particular, scientists continuously explore materials with an excellent photoelectrochemical performance and long-term stability [5].

In photoelectrocatalysis, α-Fe_2O_3 (hematite) has long been considered one of the most promising photoanode materials due to its excellent chemical stability, cost-effectiveness, and environmentally friendly properties [6–9]. As an n-type semiconductor, α-Fe_2O_3 has a suitable band gap and can theoretically provide a photocurrent density of 12.6 mA/cm^2 under AM 1.5G [4,10] (standard illumination conditions). However, despite its excellent theoretical performance, the photoelectrocatalytic efficiency of pure α-Fe_2O_3 in practical applications is still limited by several factors, including the slow kinetics of the oxygen evolution reaction, the limited hole diffusion length (around 2–4 nm), the elevated rates of carrier recombination, and poor conductivity. These limitations cause α-Fe_2O_3 to typically require an external bias voltage to enhance its performance in photoelectrochemical water-splitting reactions [11,12]. To address these challenges, other researchers have investigated various modification strategies, including altering the crystal morphology of α-Fe_2O_3 and introducing various oxygen evolution catalysts, such as Ni, Co, Ir, and Ru, for surface modification. These strategies aim to improve the photocurrent density of α-Fe_2O_3 and reduce the overpotential, thereby enhancing its photoelectrocatalytic performance. Additionally, constructing heterojunctions with other materials has become a practical modification approach [13–15]. Heterojunction structures are designed to optimize charge separation and significantly improve charge transfer efficiency between the semiconductor and the electrolyte [16,17], thereby significantly improving the photoelectrocatalytic performance. In this context, Cu_2ZnSnS_4 (CZTS) has shown great potential as a material for constructing heterojunctions with α-Fe_2O_3 [18,19]. CZTS is a p-type semiconductor composed of abundant elements in the Earth's crust, making it low-cost and non-toxic. Its band gap, ranging from 1.1 to 1.5 eV, gives it excellent light absorption capability in the visible spectrum. When combined with α-Fe_2O_3 to form a heterojunction, CZTS compensates for the shortcomings of α-Fe_2O_3, but also effectively enhances its photoelectrocatalytic performance [20,21]. Firstly, the band structure of CZTS is well matched with that of α-Fe_2O_3, which helps to form an effective band alignment, promoting charge separation and migration. Secondly, the higher light absorption capacity of CZTS can enhance the generation of photogenerated charge carriers in the heterojunction, thereby increasing the photocurrent density [22]. Additionally, the introduction of CZTS can improve the conductivity of α-Fe_2O_3, helping to reduce carrier recombination and enhance charge transfer efficiency, thereby boosting the overall catalytic performance. The heterojunction of CZTS and α-Fe_2O_3 demonstrates broad application prospects in the field of photoelectrocatalysis [23–25]. By optimizing the construction and regulation of the heterojunction, the shortcomings of α-Fe_2O_3 in photoelectrocatalysis can be effectively overcome, enabling more efficient photoelectrochemical water-splitting reactions. This strategy not only offers new approaches for enhancing the performance of α-Fe_2O_3, but also paves the way for further research and the application of photoelectrocatalytic materials [26–29].

In this study, α-Fe_2O_3 nanorod arrays loaded with CZTS substantially improved the photoelectrocatalytic performance. This indicates that the efficiency of the FC-15 material in the photoelectrocatalytic process has been significantly improved. Further studies revealed that the hole transfer efficiency of FC-15 material was approximately twice more than that of the original α-Fe_2O_3 nanorods, indicating that the introduction of the heterojunction significantly enhanced electron–hole pair separation and effectively reduced the recombination of photogenerated electrons and holes. Electrochemical Impedance Spectroscopy (EIS) analysis indicated a substantial reduction in the charge transfer resistance of the modified material, indicating that the modification enhanced the charge transport capability of the material. Band gap analysis revealed that the band gap of the modified material was reduced, which favors enhanced light absorption, and consequently improves the material's overall performance in photoelectrocatalytic reactions. These modification strategies enhanced the material's photoelectrocatalytic activity and improved its light

absorption properties and charge transport efficiency, offering better material options for photoelectrocatalytic applications.

2. Results and Discussion

2.1. Structure and Morphology

Figure 1a shows the XRD pattern of synthesized CZTS powder. By analyzing the pattern, distinct diffraction peaks can be observed at 28.530°, 44.996°, and 56.177°. By comparing these peaks with the CZTS standard reference card PDF#26-0575, they were confirmed to correspond to the characteristic peaks of the (112), (220), and (312) crystal planes of CZTS, respectively. Figure 1b shows the XRD patterns of the unmodified α-Fe_2O_3 nanorods and the FC-15 material. Significant diffraction peaks can be observed at 35.093°, 38.421°, 40.170°, 53.004°, 62.949°, 70.660°, 76.218°, and 77.368°. By comparing with the titanium (Ti) standard reference card PDF#44-1294, these peaks were identified as corresponding to the (110), (002), (101), (102), (103), (112), and (201) crystal planes of Ti, respectively. Additionally, the peak observed at 27.446° matches the TiO_2 standard reference card PDF#21-1276, corresponding to the (110) crystal plane of TiO_2, indicating that a part of the Ti substrate was oxidized to form TiO_2 during the annealing process. To further confirm the crystal phase of α-Fe_2O_3, the α-Fe_2O_3 XRD standard reference card PDF#33-0664 was consulted. Analysis shows that the diffraction peaks at 24.138°, 33.152°, 35.611°, 49.479°, and 54.089° correspond to the hematite phase of the α-Fe_2O_3 nanorods, specifically the (012), (104), (110), (024), and (116) crystal planes. However, in ref. [30], no distinct CZTS diffraction peaks were observed in the XRD pattern, likely due to the low loading amount of CZTS, which is beyond the detection limit of the XRD instrument.

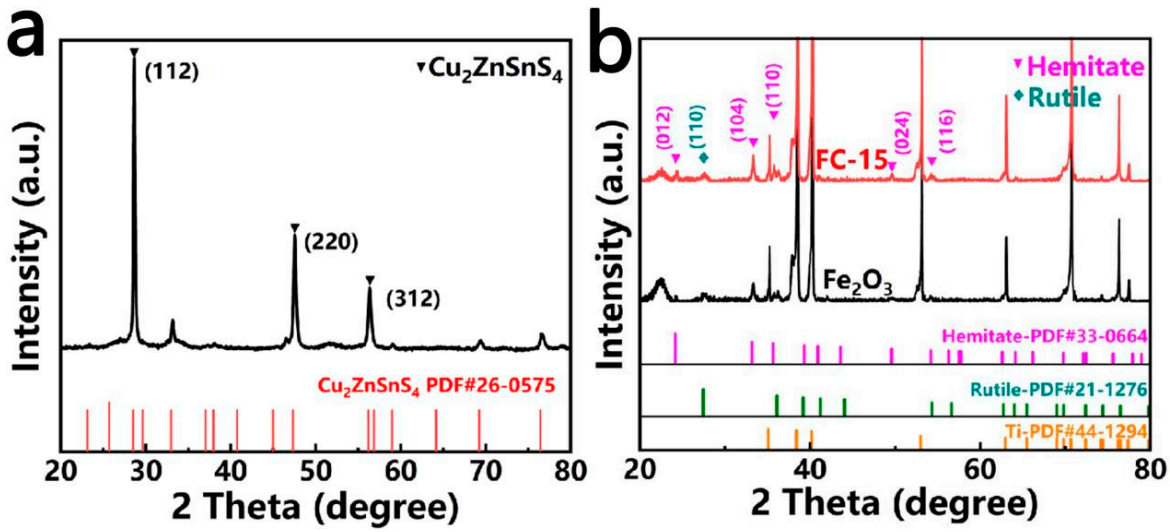

Figure 1. (**a**) CZTS powder; (**b**) XRD patterns of pure α-Fe_2O_3 nanorods and FC-15 material.

Figure 2a,c presents the SEM images of the α-Fe_2O_3 nanorods and the FC-15 material, respectively. SEM analysis indicates that both the samples exhibit similar nanorod structures, with densely packed nanorods vertically grown on the Ti substrate. Figure 2a presents an SEM image of the α-Fe_2O_3 nanorods, clearly showing their typical rod-like morphology. Figure 2c shows an SEM image of the FC-15 nanorods. Despite the CZTS modification, the nanorod morphology did not undergo significant changes, and no distinct CZTS particles were observed on the surface. This may be due to the low loading amount of CZTS, and the resolution of the SEM may not be sufficient to display the CZTS material. As seen in the images, the length of these nanorods is approximately 600–700 nm, further confirming their rod-like structural characteristics. Figure 2b,d shows side-view SEM images of the pure α-Fe_2O_3 nanorods and the FC-15 material nanorods, respectively.

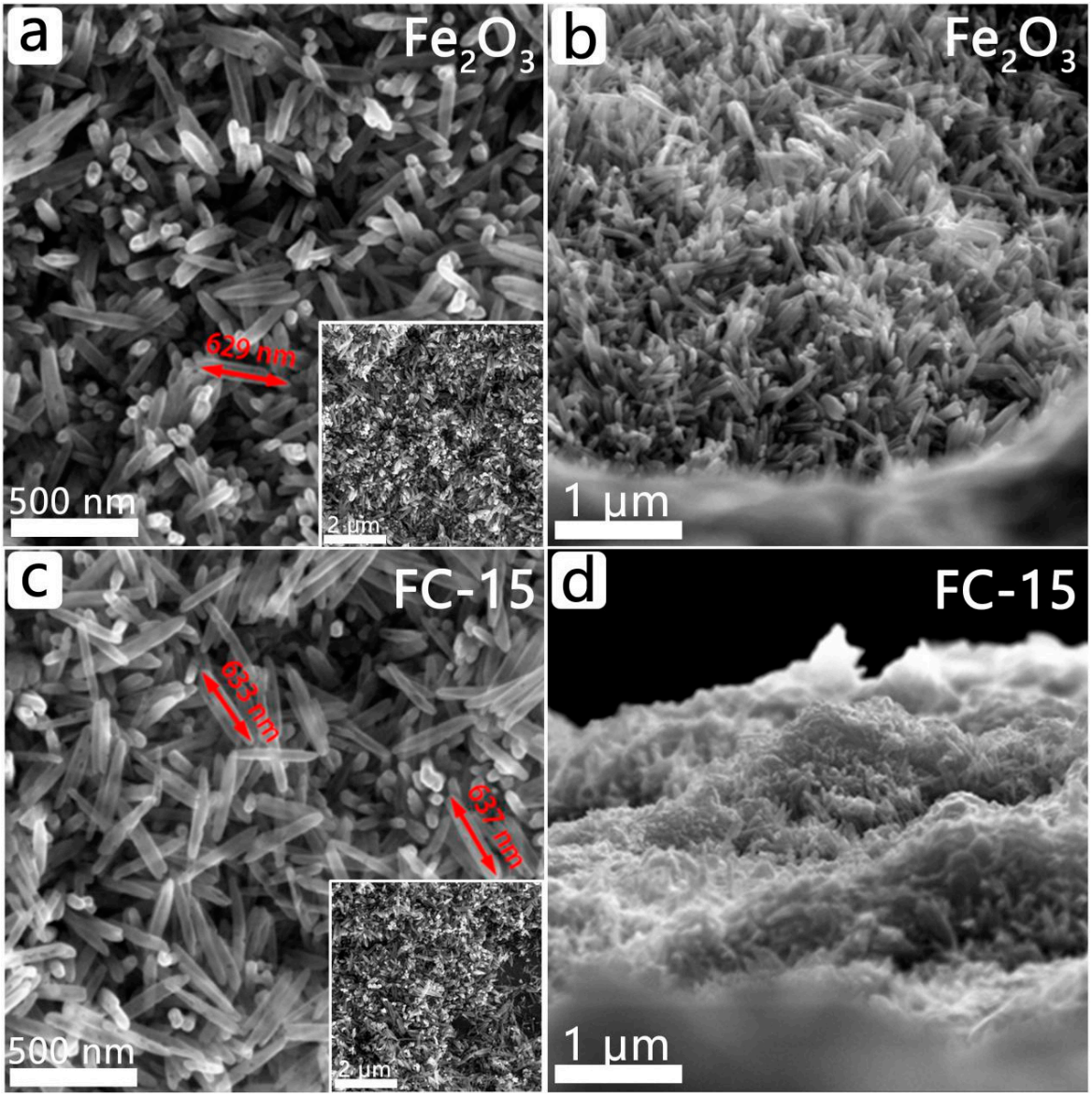

Figure 2. (**a**) α-Fe_2O_3 nanorods; (**b**) SEM images of FC-15 nanorods; (**c**) side view of α-Fe_2O_3 nanorods; (**d**) side view of FC-15 nanorods.

To further investigate the microstructure of the prepared α-Fe_2O_3 samples, transmission electron microscopy (TEM) analysis was conducted, with the results depicted in Figure 3a,c. Analysis shows that the original α-Fe_2O_3 and the FC-15 samples exhibit the same crystal structure as α-Fe_2O_3. In the TEM images of both the samples, lattice fringes corresponding to the α-Fe_2O_3 (110) crystal plane were observed, with a lattice spacing of 0.247 nm. Figure 3b,d shows a selective electron diffraction (SAED) map and Fourier transform plots of the α-Fe_2O_3 light anode. From the SAED patterns, the (012), (021), and (024) crystal planes of α-Fe_2O_3 can be indexed. Additionally, the lattice spacing of the (110) crystal plane calculated from the Fourier transform image is 0.247 nm, consistent with the data observed in the TEM images. In the TEM image of the FC-15 photoanode (Figure 3c), lattice fringes corresponding to the CZTS (110) crystal plane were also observed, with a lattice spacing of 0.384 nm. Figure 3e–j displays the EDS elemental mapping of the FC-15 photoanode, illustrating the uniform distribution of S, Sn, Zn, Fe, O, and Cu elements within the α-Fe_2O_3 nanorods. This indicates that the CZTS nanolayer was successfully loaded onto α-Fe_2O_3. Based on the characterization results, it can be inferred that the

photocatalytic performance of α-Fe_2O_3 is expected to be further enhanced through the combined effects of the heterojunction structure and the CZTS coating.

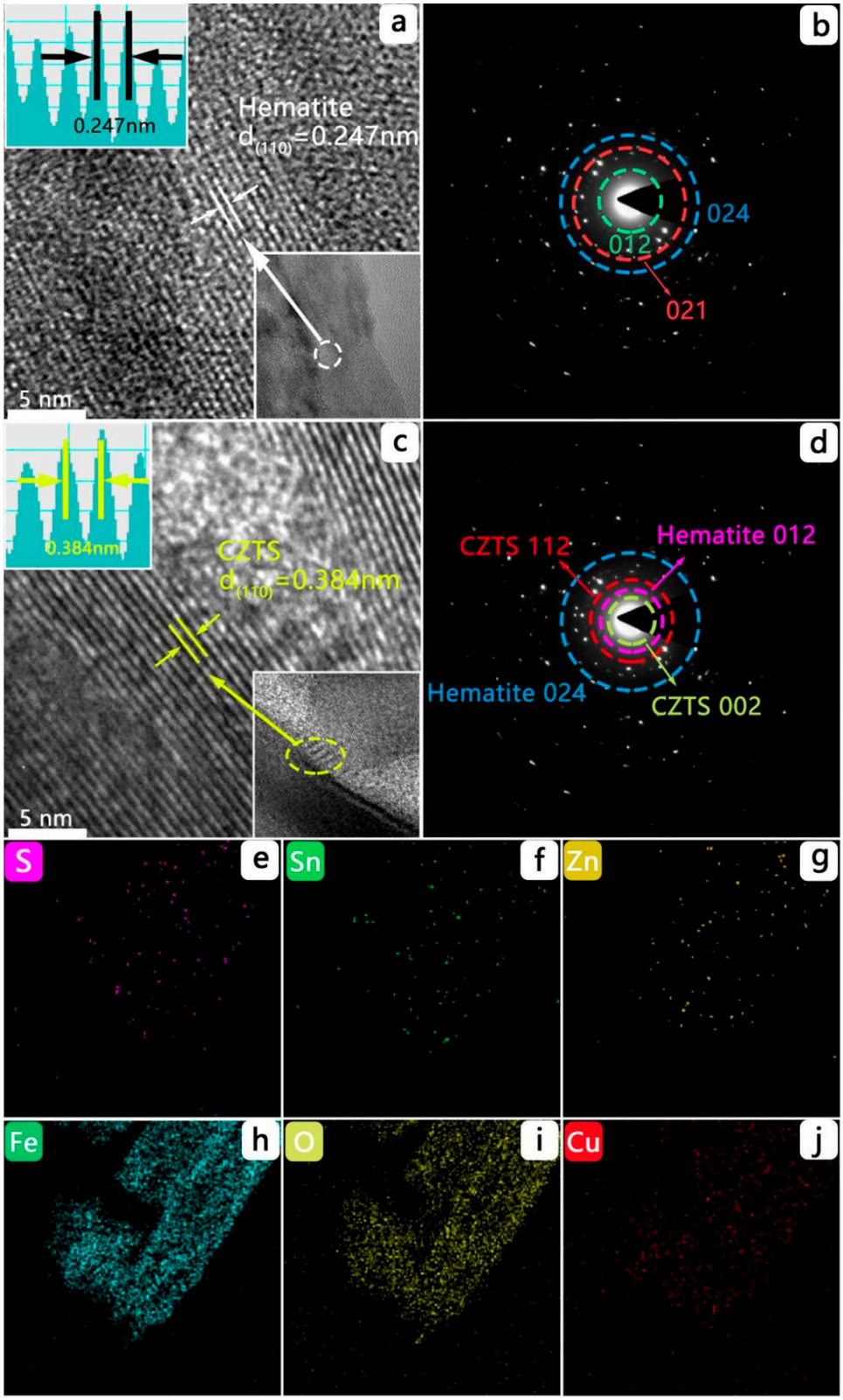

Figure 3. (**a**) TEM images of α-Fe_2O_3 nanorods; (**b**) diffraction ring pattern of α-Fe_2O_3 nanorods; (**c**) TEM images of FC-15; (**d**) diffraction ring pattern of FC-15; (**e**–**j**) elemental mapping of FC-15.

XPS analysis was performed on the α-Fe_2O_3 and FC-15 photoanodes to verify the elemental composition of the synthesized materials. Figure 4a presents the XPS spectra of Fe in the α-Fe_2O_3 and FC-15 photoanodes, displaying two peaks at binding energies (BEs) of 723.5 eV and 711.6 eV, which correspond to Fe $2p_{1/2}$ and Fe $2p_{3/2}$, respectively. Moreover, the peaks observed at 712.7 eV, 709.9 eV, 719.3 eV, and 731.6 eV further validate the existence of Fe^{3+} in the α-Fe_2O_3 photoanode. Figure 4b illustrates the O 1s spectrum, with peaks at 529.5 eV and 531.5 eV corresponding to lattice oxygen and surface-adsorbed oxygen in the α-Fe_2O_3 photoanode, respectively. The presence of these Fe and O elements confirms that the synthesized material is Fe_2O_3. The further analysis of Figure 4c–f shows the presence of Cu, Zn, Sn, and S elements on the FC-15 photoanode [31], indicating that CZTS was successfully loaded onto the FC-15 photoanode, forming a heterojunction structure with α-Fe_2O_3.

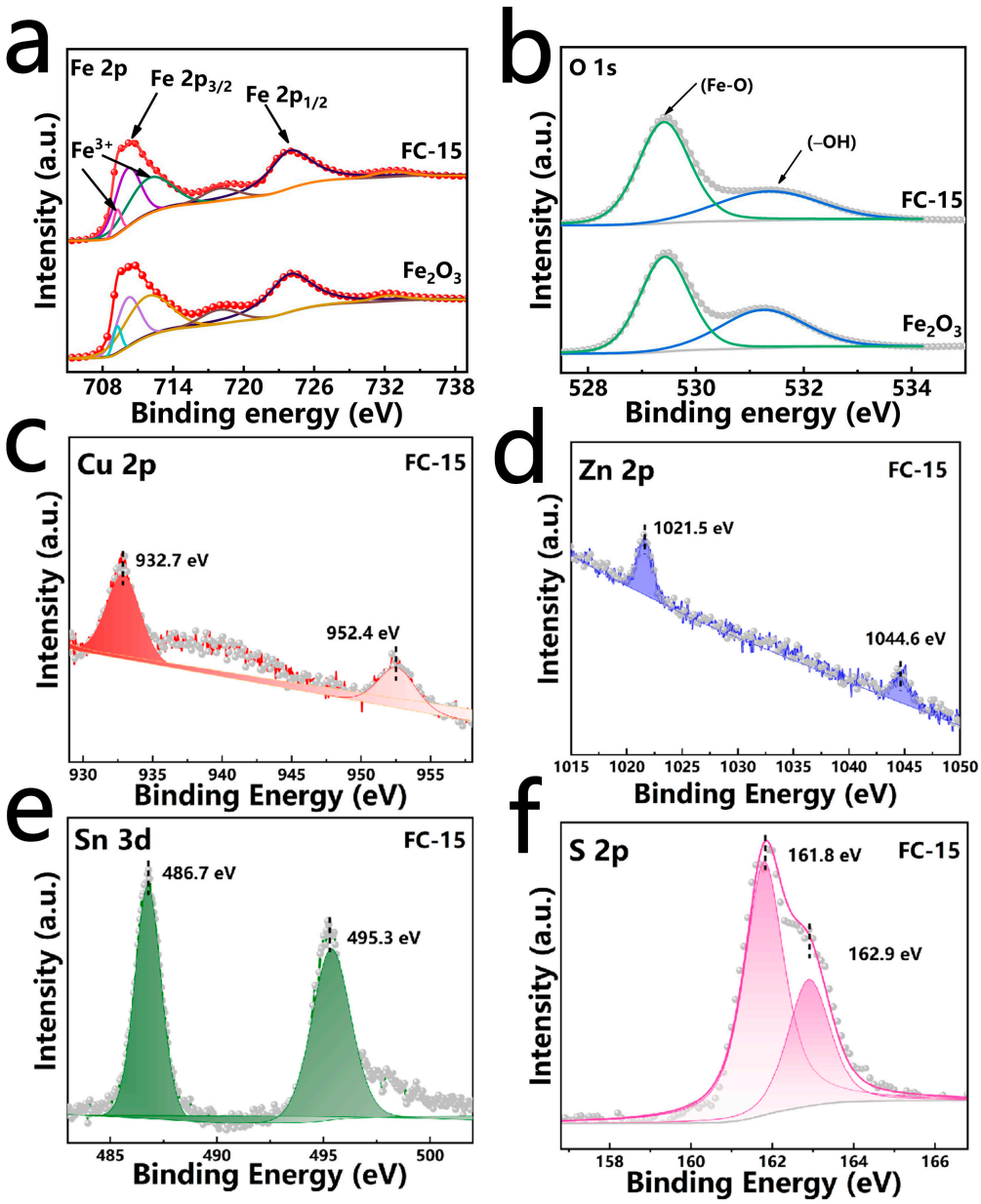

Figure 4. (**a**,**b**) XPS spectra of α-Fe_2O_3 and FC-15; (**c**) Cu 2p; (**d**) Zn 2p; (**e**) Sn 3d; (**f**) S 2p.

2.2. Photoelectrochemical Properties

The prepared photoanodes underwent testing via linear sweep voltammetry (LSV) under AM 1.5 G simulated sunlight, as illustrated in Figure 5a. At a measurement of

1.60 V vs. RHE, the FC-15 photoanode exhibited the highest photocurrent density, reaching 3.40 mA/cm^2, while the bare α-Fe_2O_3 photoanode showed the lowest photocurrent density, only 0.40 mA/cm^2. The photocurrent densities for the FC-5, FC-10, FC-20, and FC-25 photoanodes were recorded as 1.77 mA/cm^2, 2.60 mA/cm^2, 2.88 mA/cm^2, and 1.53 mA/cm^2, respectively. This indicates that the appropriate loading of CZTS can significantly enhance the photoelectrochemical performance. Additionally, Figure 5a shows that the onset potential of the modified photoanodes did not change significantly, indicating that the water oxidation kinetics of the material remained stable. Figure 5b presents the calculated results of the applied bias photon-to-current efficiency (ABPE) for the bare α-Fe_2O_3 and FC-15 photoanodes. As shown in Figure 5b, the ABPE value of the FC-15 material was significantly improved, reaching a maximum of 2.32% at 1.44 V vs. RHE. To evaluate the photoelectrocatalytic stability of the photoanodes before and after modification [32], chronoamperometry (i-t) tests were conducted on the prepared α-Fe_2O_3 and FC-15 photoanodes under AM 1.5G simulated sunlight, with an applied bias of 1.23 V vs. RHE. Figure 5c shows that the modified and unmodified photoanodes exhibited good stability. During a continuous 1 h test, the photocurrent density of the samples showed almost no decay, indicating that CZTS, as a modification material, exhibits excellent stability. Photoelectrochemical water-splitting hydrogen production tests were also conducted on the prepared α-Fe_2O_3 and FC-15 photoanodes under AM 1.5G simulated sunlight. As shown in Figure 5d, the photocatalytic hydrogen production capability of the FC-15 material was significantly enhanced [33]. After 3 h of testing, the hydrogen production rate of the FC-15 photoanode reached 41.6 μmol/cm^2/h, while the unmodified α-Fe_2O_3 photoanode exhibited a hydrogen production rate of only 5.64 μmol/cm^2/h. This outcome further highlights the effectiveness of CZTS modification in boosting the photocatalytic hydrogen production performance.

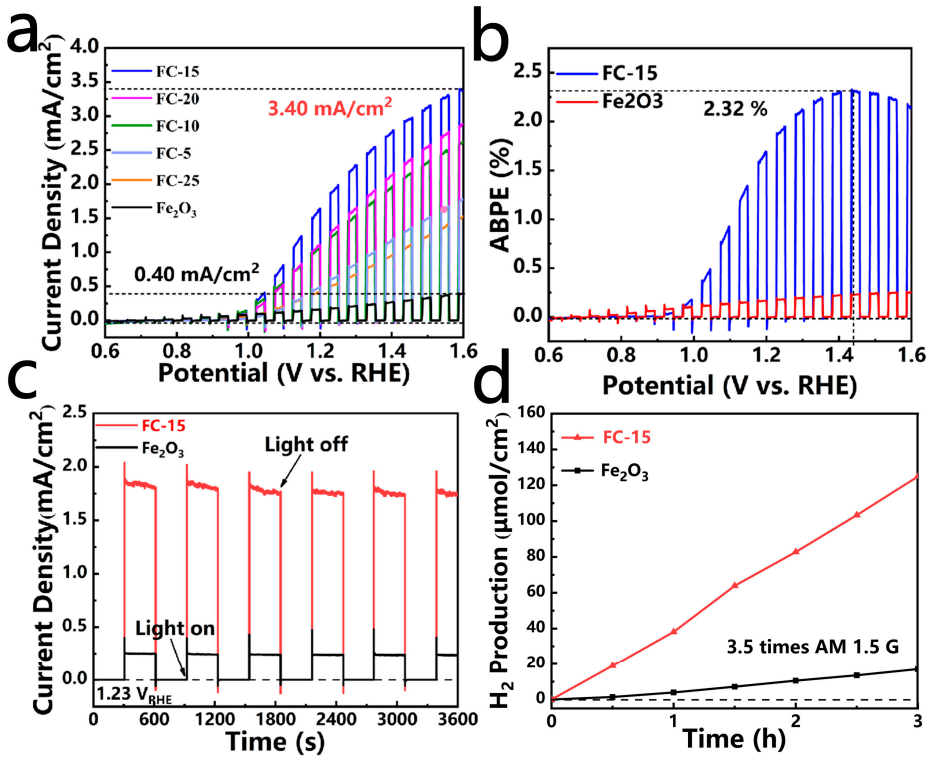

Figure 5. (**a**) LSV curves of α-Fe_2O_3, FC-5, FC-10, FC-15, FC-20, and FC-25 photoanodes; (**b**) ABPE curves of α-Fe_2O_3 and FC-15 photoanodes; (**c**) i-t curves of α-Fe_2O_3 and FC-15; (**d**) photocatalytic hydrogen production performance of α-Fe_2O_3 and FC-15 photoanodes.

The correlation between the photocurrent density of the samples and monochromatic light was evaluated using the electrochemical noise (ECN) technique. ECN is a non-

destructive in situ monitoring method frequently employed to investigate the spontaneous electrochemical reaction behavior of photoanodes. As shown in Figure 6a, the performance of FC-15 in the visible light region was significantly better than that of unmodified α-Fe_2O_3. To further investigate the monochromatic light response performance under different applied biases, the photocurrent density of the α-Fe_2O_3 and FC-15 photoanodes was tested at four different applied biases (1.0 V vs. RHE, 1.2 V vs. RHE, 1.4 V vs. RHE, and 1.6 V vs. RHE). The results are shown in Figure 6c,d. As the applied bias increased, the photocurrent density of the samples significantly improved. A higher bias improves the separation efficiency of the photogenerated electron–hole pairs in α-Fe_2O_3. Figure 6c shows incident photon-to-photocurrent density curves of the pristine α-Fe_2O_3 sample, while Figure 6d presents corresponding curves for the FC-15 sample. By comparison, the photocurrent density of the modified FC-15 photoanode showed a marked increase under every applied bias condition. Additionally, Figure 6e,f displays external quantum efficiency (IPCE) plots for the pristine α-Fe_2O_3 sample and the FC-15 sample, respectively. At an applied bias of 1.6 V vs. RHE, the IPCE value of the FC-15 sample at a wavelength of 358 nm reached 12.49%, while the pristine α-Fe_2O_3 sample exhibited an IPCE value of only 4.07% at the same wavelength. This further demonstrates that CZTS modification effectively enhanced the photoelectric response performance of the samples.

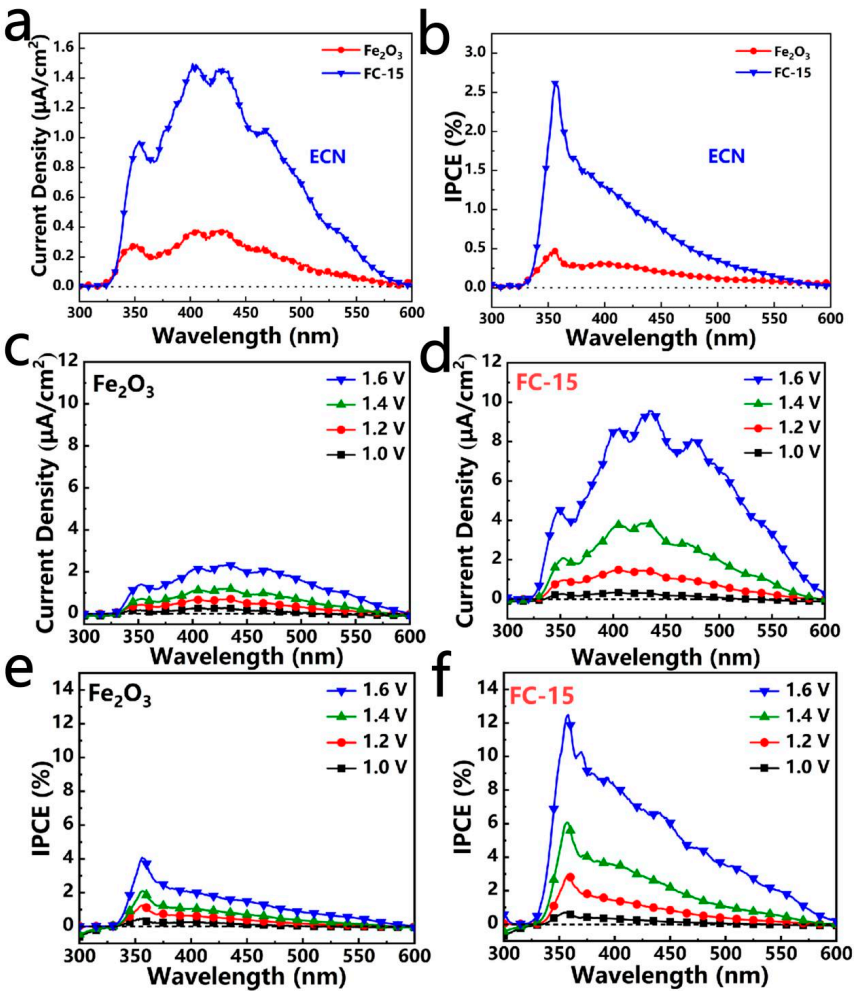

Figure 6. (**a**,**b**) The electrochemical noise patterns of pristine α-Fe_2O_3 and FC-15. (**c**) The incident photon-to-photocurrent density of the pristine α-Fe_2O_3 sample. (**d**) The incident photon-to-photocurrent density of the FC-15 sample. (**e**) An IPCE plot of the pristine α-Fe_2O_3 sample. (**f**) An IPCE plot of the FC-15 sample.

Using the IPCE test data, the band gap of the samples was estimated through Tauc plotting as a function of photon energy (*hν*), as shown in Figure 7b. After calculations, the band gap of the pristine α-Fe_2O_3 sample was found to be 2.13 eV, while the band gap of the FC-15 photoanode, which constructed a heterojunction by loading CZTS, was reduced to 2.07 eV. The smaller band gap contributes to improved light absorption capability, and this improvement boosts the photocatalytic performance of the sample. Figure S1 presents the band gap diagrams measured at various voltages. EIS tests were conducted to investigate the charge transport properties of the samples further. As illustrated in Figure 7a, the EIS diagram of the FC-15 photoanode exhibits a smaller semicircle radius, indicating less charge transfer resistance. Combined with the data from Table S1, it is evident that resistance at the electrode/electrolyte interface significantly decreases after CZTS loading. This indicates that by constructing the CZTS/α-Fe_2O_3 heterojunction, the charge transfer resistance of α-Fe_2O_3 is markedly reduced, leading to improved charge separation and transport efficiency.

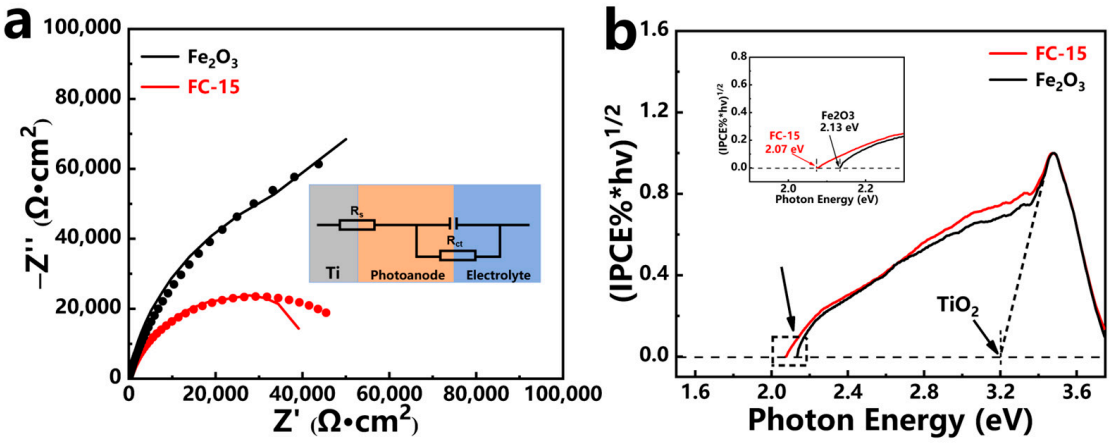

Figure 7. (**a**) The EIS spectra of the α-Fe_2O_3 and FC-15 photoanodes. (**b**) Band gap diagrams of the α-Fe_2O_3 sample and FC-15, with an inset showing a magnified view.

M-S tests were carried out on the prepared α-Fe_2O_3 and FC-15 photoanodes. As shown in Figure 8a, the slopes of the M-S curves for both the modified and unmodified samples are positive, revealing the n-type semiconductor nature of α-Fe_2O_3. Based on the data from the Mott–Schottky curves and using Equation (4), the carrier concentrations of the α-Fe_2O_3 and FC-15 photoanodes were calculated. As indicated by the values in Table S2, the carrier concentration of the unmodified α-Fe_2O_3 sample is $N_d = 0.05 \times 1020$ cm^{-3}. After loading CZTS and constructing the heterojunction, the carrier concentration increases to $N_d = 0.24 \times 1020$ cm^{-3}, demonstrating that the construction of the α-Fe_2O_3/CZTS heterojunction enhances conductivity. To demonstrate that the construction of the CZTS/α-Fe_2O_3 heterojunction promotes the separation of photogenerated electron–hole pairs, hole transfer efficiency analysis was conducted on the prepared α-Fe_2O_3 and FC-15 photoanodes. Figure 8b shows that the hole transfer efficiency gradually increases with the applied bias. This is because a higher applied bias promotes the separation of photogenerated electron–hole pairs. The maximum hole transfer efficiency of the unmodified α-Fe_2O_3 photoanode was 41.92%, while after modification, the FC-15 photoanode achieved a maximum hole transfer efficiency of 86.22%. The marked improvement in hole transfer efficiency between the photoanode and the electrolyte suggests that the heterojunction structure plays a crucial role in promoting the separation of photogenerated electron–hole pairs.

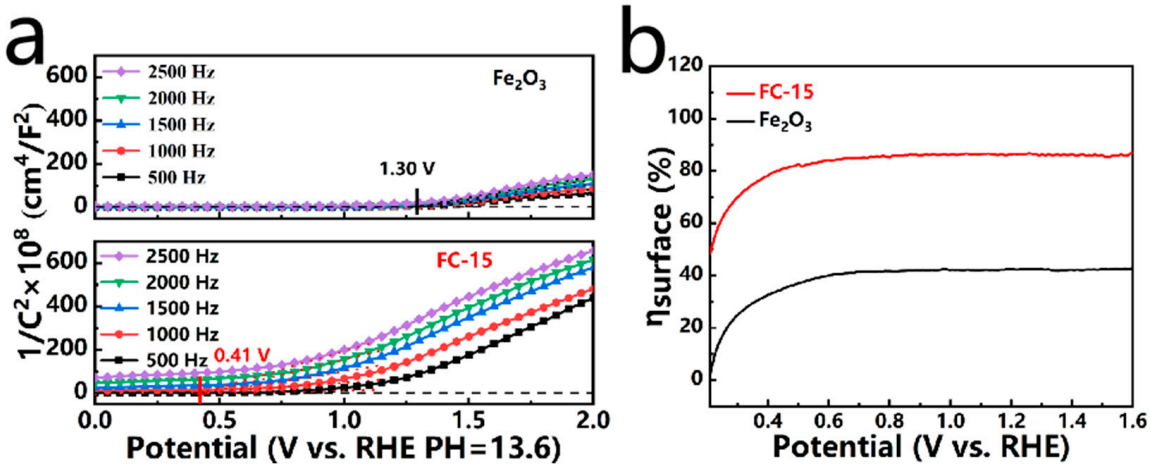

Figure 8. (**a**) Mott–Schottky (M-S) curves of α-Fe_2O_3 and FC-15 photoanodes; (**b**) η surface curves of α-Fe_2O_3 and FC-15 photoanodes.

2.3. Photoelectrochemical Water-Splitting Mechanism Under Solar Illumination

Based on the characterization and test analysis mentioned above, the photocatalytic water-splitting mechanism of the FC-15 photoanode was proposed. As shown in Figure 9, the photoanode generates electron–hole pairs under sunlight irradiation. These electron–hole pairs recombine quickly at lower bias voltages, leading to the poor photocatalytic performance of the photoanode under such conditions. As the applied bias increases, the electron–hole pairs are separated. The photogenerated electrons are transferred through the wire to the photocathode surface, reducing water to produce hydrogen, while the photogenerated holes react with water at the photoanode surface, generating oxygen. Under the influence of CZTS, a heterojunction is formed between α-Fe_2O_3 and CZTS. The internal electric field within the heterojunction promotes the separation of photogenerated electron–hole pairs, enabling more holes to participate in water oxidation and more electrons to contribute to water reduction. It was also found that after constructing the heterojunction, the carrier concentration increased, while the charge transfer resistance significantly decreased, further enabling efficient photocatalytic water splitting for hydrogen production.

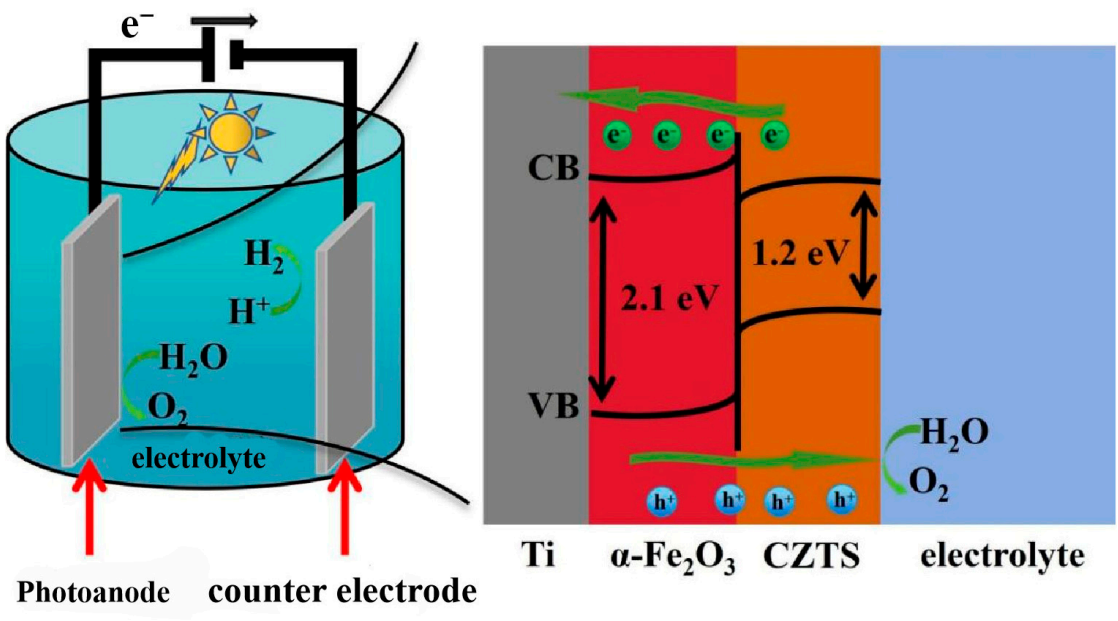

Figure 9. Mechanism of water decomposition of FC-15 photoelectric anode.

The analysis of the band structure and the partial density of states (PDOS) helps to deeply understand the electronic configuration of the α-Fe_2O_3 nanorod arrays before and after the introduction of CZTS. Using the density functional theory (DFT), detailed calculations of the electronic structure and the density of states (DOSs) were performed on the CZTS/α-Fe_2O_3 heterostructure. Figure 10a shows that original α-Fe_2O_3 exhibits a band gap of 0 eV, indicating its semimetallic nature in an unmodified state. In Figure 10b, the modified CZTS/α-Fe_2O_3 heterostructure also displays a Fermi level (E-f) of 0 eV, suggesting effective control over the electronic structure of the heterojunction interface, particularly near the Fermi level, which offers potential for optoelectronic applications such as photocatalysis and photoelectrochemistry. Figure 10c,d provides detailed presentations of the partial density of states (PDOSs) for each element within the CZTS/α-Fe_2O_3 heterostructure. For the α-Fe_2O_3 part, the d orbitals of Fe and the p orbitals of O make significant contributions near the Fermi level, indicating these orbitals play a crucial role in electronic states. In the CZTS section, the d orbitals of Cu and Zn, as well as the p orbitals of Sn, also make significant contributions to electronic state density. This orbital hybridization facilitates the separation and transmission of charge carriers, which may positively impact the photocatalytic efficiency of the heterostructure. To further elucidate the electronic alignment and photocatalytic efficiency, we applied Anderson's rule to analyze the band alignment between α-Fe_2O_3 and CZTS. This alignment suggests that the valence band maximum (VBM) of CZTS and the conduction band minimum (CBM) of α-Fe_2O_3 align favorably relative to the redox potentials required for the hydrogen evolution reaction (HER) and the oxygen evolution reaction (OER) [2,3]. This alignment supports the formation of a Z-scheme mechanism, wherein the photogenerated electrons in CZTS transfer to the α-Fe_2O_3 conduction band, while the photogenerated holes in α-Fe_2O_3 move towards the VBM of CZTS. This efficient separation and directional movement of charge carriers enhance both the HER and OER processes, thereby increasing the overall photoelectrocatalytic efficiency of the CZTS/α-Fe_2O_3 heterojunction [34,35].

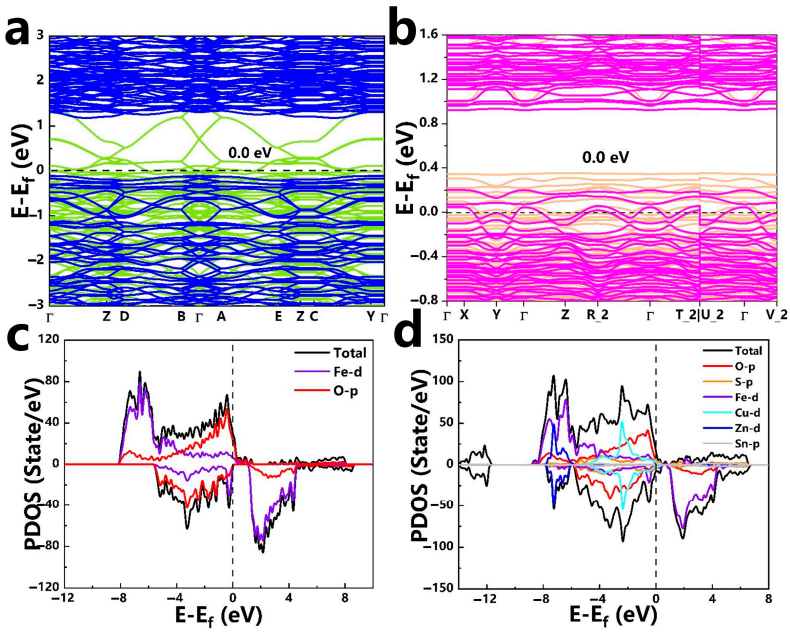

Figure 10. (**a**) Electronic band structure of α-Fe_2O_3. Green curves represent spin-up band structure while the blue curves represent spin-down bands, for accurate calculation of the band gap. (**b**) Electronic band structure of FC sample. Orange curves represent spin-up band structure while the Red curves represent spin-down bands, for accurate calculation of the band gap. (**c**) Total density of states and partial density of states of α-Fe_2O_3. (**d**) Total density of states and partial density of states of FC sample.

Figure 11a,b shows the crystal structure of the iron rod array, where Fe and O elements form an orderly framework. Figure 11c,d illustrates the structure of the iron rod array after loading with the CZTS composite material, where the Cu, Zn, Sn, and S elements form a distinct layered structure on the surface of the iron rod array [36,37]. This loading method may effectively enhance the photocatalytic performance of the material, providing improved pathways for charge separation and transport.

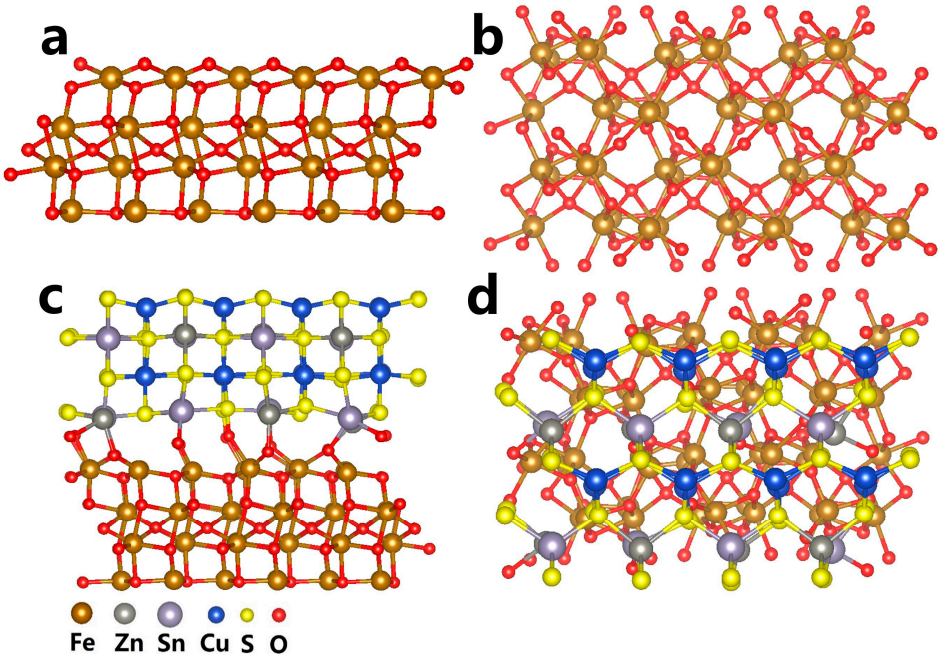

Figure 11. A schematic representation of the structures of (**a**,**b**) α-Fe_2O_3 and (**c**,**d**) the FC samples.

3. Empirical Method

3.1. Materials

Ferric chloride hexahydrate ($FeCl_3 \cdot 6H_2O$, AR), sodium nitrate ($NaNO_3$, AR), indium nitrate tetrahydrate ($In(NO_3)_3 \cdot 4.5H_2O$, AR), hydrochloric acid (HCl), acetone (C_3H_6O), anhydrous ethanol (C_2H_6O), copper(II) chloride dihydrate ($CuCl_2 \cdot 2H_2O$, AR), zinc acetate dihydrate ($Zn(CH_3OO)_2 \cdot 2H_2O$, AR), thiourea (CH_4N_2S, AR), and stannous chloride dihydrate ($SnCl_2 \cdot 2H_2O$, AR) were all purchased from Sinopharm Chemical Reagent Co., Ltd. (Shanghai, China) Pure titanium sheets were obtained from Xinji Metal Materials Co., Ltd. (Gansu, Wenchang, China)

3.2. Synthetic Method

3.2.1. Preparation of α-Fe_2O_3 Photoanodes

The preparation method of the α-Fe_2O_3 nanorod array photoanode referenced the synthesis process from the previous literature, with the main steps as follows [38,39]: First, titanium sheets were placed in a hydrochloric acid solution for ultrasonic cleaning for 1 h, followed by cleaning with a 1:1 acetone and ethanol mixed solution for 30 min. Finally, the titanium sheets were ultrasonically cleaned in laboratory-prepared ultrapure water for 30 min to ensure the surface was thoroughly clean. Subsequently, 0.015 mol of $FeCl_3 \cdot H_2O$ and 0.1 mol of $NaNO_3$ were mixed into 100 mL of deionized water, with the pH adjusted to 1.40 using hydrochloric acid. This mixture was then transferred into a stainless steel autoclave coated with polytetrafluoroethylene (PTFE), and a pre-treated titanium sheet with an approximate immersion area of 1 cm^2 was fully submerged in solution. The autoclave was subsequently placed in an oven and heated at 100 °C for 5 h to ensure proper reaction conditions. After the hydrothermal reaction, a uniform rod-shaped FeOOH structure was deposited on the surface of the Ti sheet. In order to eliminate any residual solution, the titanium sheet was carefully rinsed with ultrapure water to remove all excess materials.

The titanium sheet was placed in a muffle furnace for calcination at 550 °C for 2 h, which resulted in the formation of the α-Fe_2O_3 nanorod array photoanode.

3.2.2. The Composite of CZTS and α-Fe_2O_3 Photoanodes

CZTS powder was synthesized first [40]. $CuCl_2 \cdot 2H_2O$ (8 mM), $Zn(CH_3COO)_2 \cdot 2H_2O$ (4 mM), $SnCl_2 \cdot 2H_2O$ (4 mM), and thiourea (32 mM) were dissolved in a water and ethanol mixture (1:1). The solution was uniformly dispersed using ultrasonic treatment at room temperature for 30 min. After ensuring a homogenous mixture, it was transferred to a hydrothermal reactor and heated at 200 °C overnight. After cooling, the resulting solution was subjected to repeated centrifugation and washing. Ultimately, the powder underwent annealing in a tubular furnace at 400 °C for 2 h under an argon atmosphere, culminating in the production of CZTS powder.

Next, the synthesized CZTS powder was dispersed in ultrapure water at a 1 mM concentration and subjected to ultrasonic treatment for 1 h to achieve a homogeneous distribution. Then, a specified amount of dispersed solution was drop-cast onto the pre-prepared α-Fe_2O_3 nanorod array photoanode. To study the effects of different concentrations, comparative experiments were conducted using drop-casting volumes of 5 μL, 10 μL, 15 μL, 20 μL, and 25 μL. The resulting modified samples were named FC-5, FC-10, FC-15, FC-20, and FC-25, respectively. Finally, the CZTS/α-Fe_2O_3 heterojunction nanorod array was successfully fabricated through annealing. Figure 12 presents a schematic diagram of the preparation method.

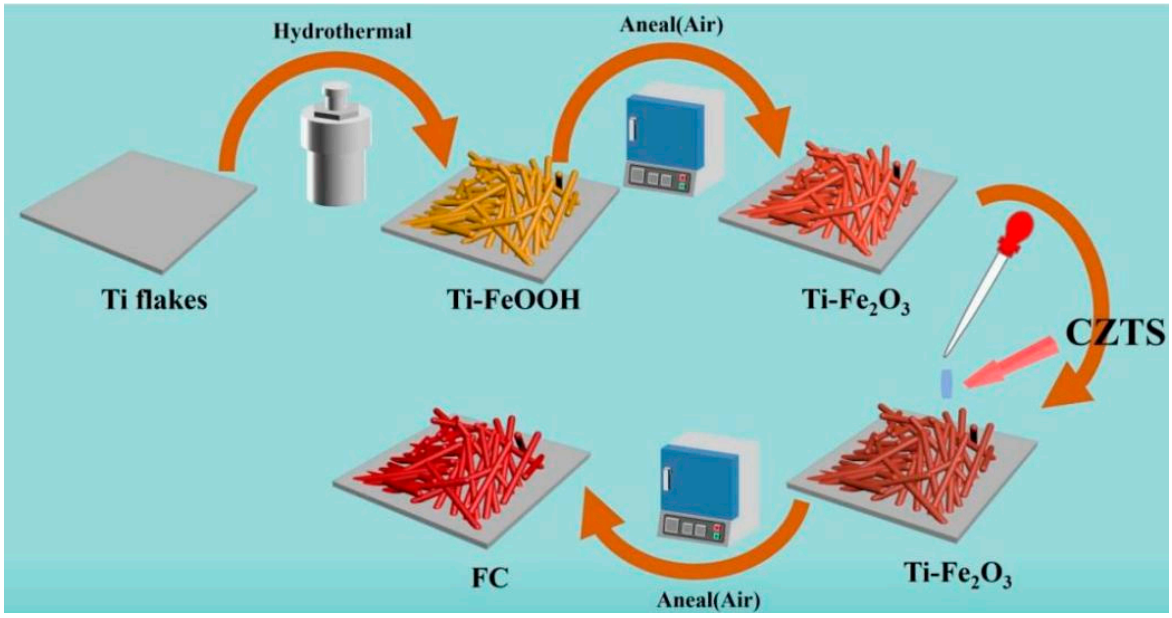

Figure 12. A flow chart of the synthesis of α-Fe_2O_3 and FC.

3.3. Material Characterization

We utilized several analytical techniques to thoroughly evaluate the material's microstructure, surface composition, and crystalline characteristics. Surface morphology observations were conducted using a scanning electron microscope (SEM, model Apreo S LoVac, Thermo Fisher Scientific, Waltham, MA, USA). For crystalline phase analysis, X-ray diffraction (XRD) was carried out using a Miniflex 600 (Rigaku, Akishima, Tokyo, Japan) employing a scan rate of 5° per minute within a 2θ range from 20° to 80°. Microstructural and elemental analyses, including transmission electron microscopy (TEM), high-resolution TEM (HRTEM), energy dispersive X-ray spectroscopy (EDS) mapping, and selected area electron diffraction (SAED), were performed using a TF 20 (Thermo Fisher Scientific, Waltham, MA, USA) at 200 kV. X-ray photoelectron spectroscopy (XPS, Thermo Scientific KAlpha, Waltham, MA, USA) with Al Kα radiation was employed for surface

chemical composition. The C 1s peak at 284.8 eV served as the reference for binding energy calibration, ensuring data accuracy. The data from XPS analysis were processed using Thermo Avantage v5.9921 (Copyright©1999–2014 Thermo Fisher Scientific portions © 1995 Micro Focus Ltd., Newbury, UK) software, applying Gaussian–Lorentzian fitting functions to derive precise surface composition values.

3.4. Photoelectrochemical (PEC) Testing

In this experiment, a quartz three-electrode electrolysis cell was used for photoelectrocatalysis. The cell had a light window on the side, allowing for xenon lamp light to directly illuminate the surface of the working electrode through the side window. The working electrode was the photoanode material prepared in this study, with an area of 1×1 cm^2. A counter electrode was made from a high-purity platinum sheet measuring 1×1 cm^2, while an Ag/AgCl electrode saturated with KCl solution was employed as the reference electrode. A total of 1 mol/L KOH solution, exhibiting a pH of 13.6, served as the electrolyte for this experiment. The photoelectrocatalytic performance of the prepared photoanode was tested using the PEC-2000 and IPCE-1000 photoelectrochemical testing systems from Perfect Light (Beijing) Co., Ltd. (Beijing, China) The PEC-2000 testing system included a CHI-760e electrochemical workstation from Shanghai Chenhua Instruments (Shanghai, China) equipped with a highly uniform integrated xenon lamp light source (model PLS-FX300HU) fitted with an AM 1.5G filter. During photoelectrocatalytic performance testing, the power of the xenon lamp was calibrated to 100 mW/cm^2. Linear sweep voltammetry (LSV) was one of the most important testing methods in this experiment. It was primarily used to characterize the photoelectrocatalytic performance of the material, demonstrating the relationship between the applied bias and the photocurrent density of the material under simulated sunlight conditions. In this experiment, the pH level of the solution can significantly influence the photoelectrocatalytic performance of the material. To eliminate this effect, the potential $E_{Ag/AgCl}$ was converted to the standard reversible hydrogen electrode (E_{RHE}) using the formula shown in Equation (1). The testing potential range was selected between 0.4 and 1.6 V vs. RHE, with a scan rate of 5 mV/s:

$$E_{RHE} = E_{Ag/AgCl} + 0.0592 \times \text{pH} + 0.197 \tag{1}$$

Additionally, the experimental data obtained from the linear sweep voltammetry (LSV) test can be used to calculate the photoconversion efficiency of the material using the formula shown in Equation (2):

$$ABPE\ (\%) = \frac{J \times (1.23 - V)}{I_0} \times 100\% \tag{2}$$

In this formula, *ABPE* represents photoconversion efficiency, *J* represents current density, *V* denotes the voltage between the working electrode and the reference electrode, and I_0 indicates the intensity of incident light. During testing, the incident light intensity was calibrated and maintained at I_0 = 100 mW/cm^2.

The photoanode's incident photon-to-current efficiency (*IPCE*) was determined using a photoelectrochemical system that included a 300 W xenon lamp, a grating monochromator to eliminate high-order diffraction, and an electrochemical workstation. The calculation formula is shown in Equation (3):

$$IPCE\ (\%) = \frac{1240 \times J}{\lambda \times I_0} \times 100\% \tag{3}$$

In this formula, *J* refers to photocurrent density, λ is a specific wavelength, and I_0 is the intensity of incident light, which was calibrated using a solar cell for specific wavelengths. Additionally, based on the test data, the material's band gap was evaluated by combining $(IPCE\% \times h\nu)^{1/2}$ with photon energy ($h\nu = 1240/\lambda$).

Based on the M-S curve data of the material, the following formula can be used to calculate the carrier concentration, which can reflect the conductivity of the material from the carrier concentration. The calculation formula is shown in Equation (4):

$$N_d = 2/ke\varepsilon\varepsilon_0 A^2 \quad (4)$$

In this formula, N_d represents the carrier concentration, k is the slope of the fitting tangent, A denotes the interface area, e stands for electron charge, ε is the relative permittivity of the material, and ε_0 refers to vacuum permittivity (dielectric constant).

4. Conclusions

In summary, α-Fe_2O_3 nanorod arrays were successfully prepared via a simple one-step hydrothermal method. The previously prepared CZTS dispersion was drop-cast onto the α-Fe_2O_3 nanorod arrays, and after thermal annealing, CZTS was successfully loaded onto the nanorod arrays, forming a heterojunction. XRD characterization confirmed the successful synthesis of α-Fe_2O_3, and after CZTS loading, no significant changes in the α-Fe_2O_3 lattice structure were observed. SEM characterization demonstrated that the nanorods densely grew on the substrate surface, and no significant changes in morphology were observed after modification. XPS analysis confirmed that the CZTS material was successfully loaded onto the α-Fe_2O_3 nanorod array. Photoelectrochemical testing and hole transfer efficiency tests of the prepared materials demonstrated that the heterojunction enabled the efficient separation of photogenerated electron–hole pairs. The EIS impedance spectra indicated that the charge transfer resistance of the modified material was significantly reduced. Band gap analysis confirmed that the band gap of the modified material was reduced, allowing for increased light absorption and an improved performance. Performance testing showed that the photocatalytic performance of the modified material was significantly enhanced. Under an applied bias of 1.60 V vs. RHE, the FC-15 photoanode achieved a photocurrent density of 3.40 mA/cm^2, which is 8.50 times greater than 0.40 mA/cm^2 observed for the unmodified α-Fe_2O_3 photoanode. The photocatalytic water-splitting hydrogen production capability was significantly improved, with the FC-15 photoanode achieving a hydrogen production rate of 41.6 μmol/cm^2/h compared to only 5.64 μmol/cm^2/h for the unmodified α-Fe_2O_3 photoanode.

Supplementary Materials: The following supporting information can be downloaded at: https://www.mdpi.com/article/10.3390/catal14110812/s1. Figure S1: A band gap diagram of the different voltages for the α-Fe_2O_3 samples and FC-15. Table S1. Fitting values of electronic components in α-Fe_2O_3 samples and FC-15 equivalent circuit. Table S2. Carrier concentration of α-Fe_2O_3 samples and FC-15.

Author Contributions: Conceptualization, Y.-X.C. and C.-Z.L.; methodology, W.C. and M.-H.J.; investigation, A.-S.S.; validation, H.-Y.S.; formal analysis, Y.Y., Y.-H.P. and R.C.; data curation, W.-H.Y.; writing—original draft preparation, W.C. and M.-H.J.; writing, reviewing, and editing, Y.-X.C. and C.-Z.L.; supervision, Y.-X.C. and C.-Z.L.; project administration, Y.-X.C. and C.-Z.L.; funding acquisition, Y.-X.C. and C.-Z.L. All authors have read and agreed to the published version of the manuscript.

Funding: This research was funded by the Natural Science Foundation of Fujian Province (2023H0046) and the XMIREM autonomously deployment project (2023CX10, 2023GG01).

Data Availability Statement: The original contributions presented in this study are included in this article/Supplementary Materials; further inquiries can be directed to the corresponding author.

Conflicts of Interest: The authors declare no conflicts of interest.

References

1. Tang, C.; Zhou, G.; Chen, J.; Li, Q.; Liu, C.; Wang, T.; Li, X.; Wen, S.; Zhang, L. In-Situ Localization of $Cd_{0.5}Zn_{0.5}S$ onto COFs-Derived Frameworks via Interface N Bridging Strategy for Highly Efficient Photocatalytic Hydrogen Production. *Fuel* **2025**, *381*, 133399. [CrossRef]
2. Garcia, V.G.; Inacio, G.J.; Filho, L.F.; Pacheco, L.T.; Pansini, F.N.N.; Menezes, M.G.; Paz, W.S. Exploring the Potential of α-Ge(111) Monolayer in Photocatalytic Water Splitting for Hydrogen Production. *FlatChem* **2024**, *48*, 100753. [CrossRef]

3. Procopio, E.F.; Pedrosa, R.N.; L. De Souza, F.A.; Paz, W.S.; Scopel, W.L. Tuning the Photocatalytic Water-Splitting Capability of Two-Dimensional α-In_2Se_3 by Strain-Driven Band Gap Engineering. *Phys. Chem. Chem. Phys.* **2020**, *22*, 3520–3526. [CrossRef] [PubMed]
4. Carminati, S.A.; Da Silva, B.L.; Bott-Neto, J.L.; De Melo, M.A.; Galante, M.T.; Fernández, P.S.; Longo, C.; Bonacin, J.A.; Nogueira, A.F. Hematite Nanorods Photoanodes Decorated by Cobalt Hexacyanoferrate: The Role of Mixed Oxidized States on the Enhancement of Photoelectrochemical Performance. *ACS Appl. Energy Mater.* **2020**, *3*, 10097–10107. [CrossRef]
5. Liu, J.; Liu, Y.; Liu, N.; Han, Y.; Zhang, X.; Huang, H.; Lifshitz, Y.; Lee, S.-T.; Zhong, J.; Kang, Z. Metal-Free Efficient Photocatalyst for Stable Visible Water Splitting via a Two-Electron Pathway. *Science* **2015**, *347*, 970–974. [CrossRef]
6. Chong, R.; Wang, B.; Su, C.; Li, D.; Mao, L.; Chang, Z.; Zhang, L. Dual-Functional CoAl Layered Double Hydroxide Decorated α-Fe_2O_3 as an Efficient and Stable Photoanode for Photoelectrochemical Water Oxidation in Neutral Electrolyte. *J. Mater. Chem. A* **2017**, *5*, 8583–8590. [CrossRef]
7. Wu, J.; Qi, M.; Wang, G.; Yu, B.; Liu, C.; Hou, W.; Liu, W. Synergistic Effect of Metal-Organic Framework-Derived TiO_2 Nanoparticles and an Ultrathin Carbon Layer on Passivation of Hematite Surface States. *ACS Sustain. Chem. Eng.* **2020**, *8*, 5200–5208. [CrossRef]
8. Deng, J.; Zhuo, Q.; Lv, X. Hierarchical TiO_2/Fe_2O_3 Heterojunction Photoanode for Improved Photoelectrochemical Water Oxidation. *J. Electroanal. Chem.* **2019**, *835*, 287–292. [CrossRef]
9. Cots, A.; Gómez, R. Ytterbium Modification of Pristine and Molybdenum-Modified Hematite Electrodes as a Strategy for Efficient Water Splitting Photoanodes. *Appl. Catal. B Environ.* **2017**, *219*, 492–500. [CrossRef]
10. Yuan, Y.; Gu, J.; Ye, K.-H.; Chai, Z.; Yu, X.; Chen, X.; Zhao, C.; Zhang, Y.; Mai, W. Combining Bulk/Surface Engineering of Hematite To Synergistically Improve Its Photoelectrochemical Water Splitting Performance. *ACS Appl. Mater. Interfaces* **2016**, *8*, 16071–16077. [CrossRef]
11. Shen, S.; Lindley, S.A.; Chen, X.; Zhang, J.Z. Hematite Heterostructures for Photoelectrochemical Water Splitting: Rational Materials Design and Charge Carrier Dynamics. *Energy Environ. Sci.* **2016**, *9*, 2744–2775. [CrossRef]
12. Hu, X.; Huang, J.; Cao, Y.; He, B.; Cui, X.; Zhu, Y.; Wang, Y.; Chen, Y.; Yang, Y.; Li, Z.; et al. Photothermal-boosted Polaron Transport in Fe_2O_3 Photoanodes for Efficient Photoelectrochemical Water Splitting. *Carbon Energy* **2023**, *5*, e369. [CrossRef]
13. Yang, Q.; Du, J.; Li, J.; Wu, Y.; Zhou, Y.; Yang, Y.; Yang, D.; He, H. Thermodynamic and Kinetic Influence of Oxygen Vacancies on the Solar Water Oxidation Reaction of α-Fe_2O_3 Photoanodes. *ACS Appl. Mater. Interfaces* **2020**, *12*, 11625–11634. [CrossRef]
14. Liao, A.; He, H.; Tang, L.; Li, Y.; Zhang, J.; Chen, J.; Chen, L.; Zhang, C.; Zhou, Y.; Zou, Z. Quasi-Topotactic Transformation of FeOOH Nanorods to Robust Fe_2O_3 Porous Nanopillars Triggered with a Facile Rapid Dehydration Strategy for Efficient Photoelectrochemical Water Splitting. *ACS Appl. Mater. Interfaces* **2018**, *10*, 10141–10146. [CrossRef] [PubMed]
15. Iandolo, B.; Zäch, M. Enhanced Water Splitting on Thin-Film Hematite Photoanodes Functionalized with Lithographically Fabricated Au Nanoparticles. *Aust. J. Chem.* **2012**, *65*, 633. [CrossRef]
16. Kodan, N.; Agarwal, K.; Mehta, B.R. All-Oxide α-Fe_2O_3/H:TiO_2 Heterojunction Photoanode: A Platform for Stable and Enhanced Photoelectrochemical Performance through Favorable Band Edge Alignment. *J. Phys. Chem. C* **2019**, *123*, 3326–3335. [CrossRef]
17. Hou, Y.; Zuo, F.; Dagg, A.; Feng, P. Visible Light-Driven α-Fe_2O_3 Nanorod/Graphene/$BiV_{1-x}Mo_xO_4$ Core/Shell Heterojunction Array for Efficient Photoelectrochemical Water Splitting. *Nano Lett.* **2012**, *12*, 6464–6473. [CrossRef]
18. Kuang, P.; Zhang, L.; Cheng, B.; Yu, J. Enhanced Charge Transfer Kinetics of Fe_2O_3/CdS Composite Nanorod Arrays Using Cobalt-Phosphate as Cocatalyst. *Appl. Catal. B Environ.* **2017**, *218*, 570–580. [CrossRef]
19. Natarajan, K.; Saraf, M.; Mobin, S.M. Visible-Light-Induced Water Splitting Based on a Novel α-Fe_2O_3/CdS Heterostructure. *ACS Omega* **2017**, *2*, 3447–3456. [CrossRef]
20. Liu, J.; Chen, W.; Sun, Q.; Zhang, Y.; Li, X.; Wang, J.; Wang, C.; Yu, Y.; Wang, L.; Yu, X. Oxygen Vacancies Enhanced $WO_3/BiVO_4$ Photoanodes Modified by Cobalt Phosphate for Efficient Photoelectrochemical Water Splitting. *ACS Appl. Energy Mater.* **2021**, *4*, 2864–2872. [CrossRef]
21. Xiao, J.; Fan, L.; Huang, Z.; Zhong, J.; Zhao, F.; Xu, K.; Zhou, S.-F.; Zhan, G. Functional Principle of the Synergistic Effect of Co-Loaded Co-Pi and FeOOH on Fe_2O_3 Photoanodes for Photoelectrochemical Water Oxidation. *Chin. J. Catal.* **2020**, *41*, 1761–1771. [CrossRef]
22. Xia, J.; Yan-Xin, C.; Can-Zhong, L. Bio-Inspired Materials for Photocatalytic Hydrogen Production. *Chin. J. Struct. Chem.* **2020**, *39*, 2123–2130. [CrossRef]
23. Bhoi, Y.P.; Mishra, B.G. Single Step Combustion Synthesis, Characterization and Photocatalytic Application of α-Fe_2O_3-Bi_2S_3 Heterojunctions for Efficient and Selective Reduction of Structurally Diverse Nitroarenes. *Chem. Eng. J.* **2017**, *316*, 70–81. [CrossRef]
24. Yi, S.; Wulan, B.; Yan, J.; Jiang, Q. Highly Efficient Photoelectrochemical Water Splitting: Surface Modification of Cobalt-Phosphate-Loaded Co_3O_4/Fe_2O_3 p–n Heterojunction Nanorod Arrays. *Adv. Funct. Mater.* **2019**, *29*, 1801902. [CrossRef]
25. Chen, C.; Duan, F.; Zhao, S.; Wang, W.; Yang, F.; Nuansing, W.; Zhang, B.; Qin, Y.; Knez, M. Porous Fe_2O_3 Nanotubes with α-γ Phase Junction for Enhanced Charge Separation and Photocatalytic Property Produced by Molecular Layer Deposition. *Appl. Catal. B Environ.* **2019**, *248*, 218–225. [CrossRef]
26. Ali, A.M.; Sayed, M.A.; Algarni, H.; Ganesh, V.; Aslam, M.; Ismail, A.A.; El-Bery, H.M. Synthesis, Characterization and Photoelectric Properties of Fe_2O_3 Incorporated TiO_2 Photocatalyst Nanocomposites. *Catalysts* **2021**, *11*, 1062. [CrossRef]

27. Qasim, M.; Ghanem, M.A.; Cao, X.; Li, X. Modification of α-Fe_2O_3 Nanoparticles with Carbon Layer for Robust Photo-Fenton Catalytic Degradation of Methyl Orange. *Catalysts* **2024**, *14*, 393. [CrossRef]
28. Pan, J.-B.; Liu, X.; Wang, B.-H.; Chen, Y.-A.; Tan, H.-Y.; Ouyang, J.; Zhou, W.; Shen, S.; Chen, L.; Au, C.-T.; et al. Conductive MOFs Coating on Hematite Photoanode for Activity Boost via Surface State Regulation. *Appl. Catal. B Environ.* **2022**, *315*, 121526. [CrossRef]
29. Wang, Z.; Gu, Y.; Zheng, L.; Hou, J.; Zheng, H.; Sun, S.; Wang, L. Machine Learning Guided Dopant Selection for Metal Oxide-Based Photoelectrochemical Water Splitting: The Case Study of Fe_2O_3 and CuO. *Adv. Mater.* **2022**, *34*, 2106776. [CrossRef]
30. Xie, M.; Ji, X.; Meng, H.; Jiang, N.; Luo, Z.; Huang, Q.; Sun, G.; Zhang, Y.; Xiao, P. The Role of Titanium at the Interface of Hematite Photoanode in Multisite Mechanism: Reactive Site or Cocatalyst Site? *Chin. J. Catal.* **2024**, *64*, 77–86. [CrossRef]
31. Suryawanshi, M.P.; Ghorpade, U.V.; Shin, S.W.; Gang, M.G.; Wang, X.; Park, H.; Kang, S.H.; Kim, J.H. Enhanced Solar Water Oxidation Performance of TiO_2 via Band Edge Engineering: A Tale of Sulfur Doping and Earth-Abundant CZTS Nanoparticles Sensitization. *ACS Catal.* **2017**, *7*, 8077–8089. [CrossRef]
32. Chen, D.; Liu, Z.; Zhang, S. Enhanced PEC Performance of Hematite Photoanode Coupled with Bimetallic Oxyhydroxide NiFeOOH through a Simple Electroless Method. *Appl. Catal. B Environ.* **2020**, *265*, 118580. [CrossRef]
33. Wang, Z.-Y.; Li, H.-M.; Yi, S.-S.; You, M.-Z.; Jing, H.-J.; Yue, X.-Z.; Zhang, Z.-T.; Chen, D.-L. In-Situ Coating of Multifunctional FeCo-Bimetal Organic Framework Nanolayers on Hematite Photoanode for Superior Oxygen Evolution. *Appl. Catal. B Environ.* **2021**, *297*, 120406. [CrossRef]
34. Lu, Z.; Gong, W.; Chen, J.; Guo, P.; Zhang, Y.; Zhang, L.; Yan, M.; Wu, C.; Sun, M.; Su, G.; et al. Molten Salt-Assisted Synthesis of Ferric Oxide/M–N–C Nanosheet Electrocatalysts for Efficient Oxygen Reduction Reaction. *Small Methods* **2024**, 2401278. [CrossRef]
35. Xuan, C.; Shen, T.; Hou, B. Ni/Fe_2O_3 Mott-Schottky Heterointerface Engineering and Phosphate Doping Synergistically Refining d-Band Center for Efficient Oxygen Evolution Reaction. *Chem. Eng. J.* **2024**, *479*, 147723. [CrossRef]
36. Idisi, D.O.; Ahia, C.C.; Meyer, E.L.; Bodunrin, J.O.; Benecha, E.M. Graphene Oxide: Fe_2O_3 Nanocomposites for Photodetector Applications: Experimental and *Ab Initio* Density Functional Theory Study. *RSC Adv.* **2023**, *13*, 6038–6050. [CrossRef]
37. Xu, H.-M.; Yue, K.-H.; Song, L.-J.; Zhang, H.-C.; Zhu, H.-R.; Zhang, Z.-J.; Li, G.-R. The Asymmetrical Fe-O-Se Bonds in $Fe_2O(SeO_3)_2$ Boosting Bifunctional Oxygen Electrocatalytic Performance for Zinc-Air Battery. *Angew. Chem. Int. Ed.* **2024**, e202412025. [CrossRef]
38. Koh, T.S.; Anushkkaran, P.; Hwang, J.B.; Choi, S.H.; Chae, W.-S.; Lee, H.H.; Jang, J.S. Magnetron Sputtered Al Co-Doped with Zr-Fe_2O_3 Photoanode with Fortuitous Al_2O_3 Passivation Layer to Lower the Onset Potential for Photoelectrochemical Solar Water Splitting. *Catalysts* **2022**, *12*, 1467. [CrossRef]
39. Dhandole, L.K.; Koh, T.S.; Anushkkaran, P.; Chung, H.-S.; Chae, W.-S.; Lee, H.H.; Choi, S.H.; Cho, M.; Jang, J.S. Enhanced Charge Transfer with Tuning Surface State in Hematite Photoanode Integrated by Niobium and Zirconium Co-Doping for Efficient Photoelectrochemical Water Splitting. *Appl. Catal. B Environ.* **2022**, *315*, 121538. [CrossRef]
40. Li, K.-X.; Li, C.-H.; Shi, H.-Y.; Chen, R.; She, A.-S.; Yang, Y.; Jiang, X.; Chen, Y.-X.; Lu, C.-Z. A Convenient In Situ Preparation of Cu_2ZnSnS_4-Anatase Hybrid Nanocomposite for Photocatalysis/Photoelectrochemical Water-Splitting Hydrogen Production. *Molecules* **2024**, *29*, 2514. [CrossRef]

Disclaimer/Publisher's Note: The statements, opinions and data contained in all publications are solely those of the individual author(s) and contributor(s) and not of MDPI and/or the editor(s). MDPI and/or the editor(s) disclaim responsibility for any injury to people or property resulting from any ideas, methods, instructions or products referred to in the content.